BEHAVIOUR OF SECONDARY CURRENTS IN THE LIMIT OF VANISHING RIDGE HEIGHT

Oleksandr Zhdanov
Department of Numerical Fluid Dynamics
Technical University Berlin
Berlin, Germany, 10623
oleksandr.zhdanov@tu-berlin.de

Angela Busse
Department of Numerical Fluid Dynamics
Technical University Berlin
Berlin, Germany, 10623
angela.busse@tu-berlin.de

ABSTRACT

The dependency of ridge-induced Prandtl's secondary currents of the second kind on the ridge height h is investigated for smooth sinusoidal ridges using direct numerical simulations. The ridge height is varied by over an order of magnitude from $h/\delta = 0.312 \ldots 0.00975$ at fixed spanwise wavelength $\lambda_y = 1.56\delta$, where δ is the mean half-channel height. For high to moderate ridge heights results show a close to linear decrease of the roughness function as the ridge height is reduced and a logarithmic dependency of the peak dispersive shear stress on h. As the height of the rigde is decreased to very low values of the order of the thickness of the viscous sub-layer, a departure from the linear behaviour is observed combined with an increased sensitivity of the Reynolds and dispersive stress statistics on the length of the time-averaging window and its position in time. Results for very low ridge heights indicate that – while the ridges may still be able to introduce weak secondary current-like structures in the mean flow – their height is too low to lock these structures in place, leading to increased meandering of the generated secondary current structures.

INTRODUCTION

Rough surfaces with spanwise heterogeneity are widely known to induce secondary currents of Prandtl's second kind (Prandtl, 1952), which emerge due to turbulence anisotropy and spatial gradients of the Reynolds stresses. These secondary currents are typically represented by a pair of streamwise aligned vortices separated by high- and low-momentum pathways. One class of roughness that generates secondary currents is characterised by a spanwise variation in surface topography and is commonly referred to as ridge-type roughness (Wang & Cheng, 2006). For this type of surface, the spacing between adjacent ridges has been identified as a key parameter that governs the size and strength of secondary currents (Vanderwel & Ganapathisubramani, 2015). In particular, when the ridge spacing becomes comparable to the outer length scale of the flow, the secondary current vortices become space filling. Ridge width also impacts the strength of secondary currents, which weaken as the ridges become wider (Zhdanov *et al.*, 2024). In addition, while secondary currents can be generated by any ridge shape, their topology and strength are affected by the ridge geometry (Wang & Cheng, 2006).

While most studies on ridge-type roughness have examined the impact of the aforementioned parameters on secondary currents, to the best of the authors' knowledge, the influence of ridge height has not yet been systematically explored. In particular, it remains to be established whether secondary currents can be generated by any ridge height, i.e., what is the minimum ridge height required to induce secondary currents, and the behaviour of secondary currents as the smooth-wall limit is approached by reducing the ridge height. The present study aims to address these questions. To this end, a series of direct numerical simulations of flow over ridge-type roughness with systematically varied height at constant spanwise spacing is conducted to obtain mean flow properties and turbulence statistics characterising the induced secondary currents. The ridge-type roughness is represented by a spanwise sine wave, which provides a continuous and differentiable surface without singularities avoiding the generation of corner vortices, unlike triangular or rectangular ridge shapes which have been widely used in previous studies.

METHODOLOGY

The present ridge-type roughness is described by a cosine function $h(y) = A\cos\left(\frac{2\pi y}{\lambda_y}\right)$, where A is the amplitude of the sine wave (half of the peak-to-trough roughness height h) and λ_y is the wavelength in the spanwise direction (see Figure 1). The wavelength is fixed at $\lambda_y/\delta = 1.56$, where δ is the mean half-channel height. Based on the results for triangular ridges (see, e.g., Zampiron *et al.*, 2020; Zhdanov *et al.*, 2024), this value of λ_y is expected to produce pronounced space-filling secondary currents. To date, six surfaces with systematically varied wave height ($h = 2A$) have been considered. Starting from $h/\delta = 0.312$ for case 1, the height was progressively reduced by factors of 2, reaching its minimum $h/\delta = 0.00975$ for case 6.

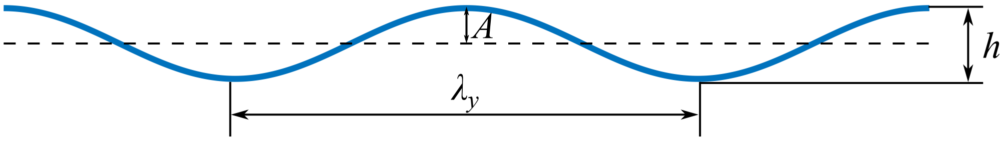

Figure 1. Schematic of the sinusoidal ridge-type roughness. A is the amplitude of the sine wave; h is the sine wave height; λ_y is the spanwise wavelength. The dashed horizontal line shows the location of the reference plane $z = 0$.

Table 1. Simulation parameters: h is the peak-to-trough roughness height ($h = 2A$); λ_y is the wavelength of the sine wave in the spanwise direction; L_x, L_y, and L_z are domain sizes in the streamwise, spanwise, and wall-normal directions; N_x, N_y, and N_z are the number of grid points in the streamwise, spanwise, and wall-normal directions; Δx^+ and Δy^+ are the viscous scaled grid spacings in the streamwise and spanwise directions; Δz^+_{min} and Δz^+_{max} are the minimum and maximum viscous scaled grid spacings in the wall-normal direction.

Case	h/δ	λ_y/δ	$L_x \times L_y \times L_z$	$N_x \times N_y \times N_z$	Δx^+	Δy^+	$\Delta z^+_{\mathrm{min}}$	$\Delta z^+_{\mathrm{max}}$
1	0.312	1.56	$6.24\delta \times 3.12\delta \times 1.156\delta$	$768 \times 384 \times 432$	4.47	4.47	0.67	4.68
2	0.156	1.56	$6.24\delta \times 3.12\delta \times 1.078\delta$	$768 \times 384 \times 336$	4.47	4.47	0.67	4.19
3	0.078	1.56	$6.24\delta \times 3.12\delta \times 1.039\delta$	$768 \times 384 \times 288$	4.47	4.47	0.67	4.00
4	0.039	1.56	$6.24\delta \times 3.12\delta \times 1.0195\delta$	$768 \times 384 \times 240$	4.47	4.47	0.67	4.53
5	0.0195	1.56	$6.24\delta \times 3.12\delta \times 1.00957\delta$	$768 \times 384 \times 224$	4.47	4.47	0.67	4.59
6	0.00975	1.56	$6.24\delta \times 3.12\delta \times 1.004875\delta$	$768 \times 384 \times 224$	4.47	4.47	0.67	4.39
smooth	-	-	$6.24\delta \times 3.12\delta \times 1\delta$	$768 \times 384 \times 240$	4.47	4.47	0.50	4.22

For each case, a DNS of a fully developed turbulent channel flow is performed at a constant friction Reynolds number $Re_\tau = u_\tau\delta/\nu = 550$, where u_τ is the mean friction velocity and ν is the kinematic viscosity, using the code iIMB (Busse *et al.*, 2015). The flow in the channel is driven by a constant mean streamwise pressure gradient. The simulations were performed in a half-channel configuration, i.e., the ridge-type roughness is placed on the bottom channel wall and a free-slip boundary condition is set at the top plane of the channel. The geometry of the ridges is resolved using an iterative version of the embedded boundary method (Yang & Balaras, 2006) and their surface is treated as the no-slip wall. Periodic boundary conditions are imposed in the streamwise and spanwise directions.

The channel size is set to $6.24\delta \times 3.12\delta$ in the streamwise (x) and spanwise (y) direction. In the wall-normal (z) direction, the computational domain size L_z is set to $(\delta + A)$, so that the reference plane $z = 0$ corresponds to the mean roughness height and the mean half-channel height is δ for all cases. The grid spacing is uniform in the streamwise and spanwise directions with $\Delta x^+ = \Delta y^+ = 4.47$. In the wall-normal direction, the computational grid is uniform with $\Delta z^+_{\mathrm{min}} = 2/3$ across the sine wave height, and is gradually stretched above reaching $\Delta z^+_{\mathrm{max}} < 5$ at channel centre. A reference smooth wall simulation is also performed in a half-channel configuration for the same Re_τ and domain size. The simulation parameters are summarised in Table 1. In each case, the flow statistics are acquired for a minimum of 200 flow through times after the initial transient. The double-averaging approach of Raupach & Shaw (1982) is used to compute statistical quantities.

RESULTS AND DISCUSSION

The contours of mean streamwise velocity fields together with in-plane velocity vectors for cases 1, 3, 5, and 6 are presented in Figure 2. As expected, tall and medium sinusoidal ridges (cases 1–4) induce a pair of space-filling counter-rotating secondary current vortices. The observed topology of secondary currents represents a typical topology reported for ridge-type roughness (e.g., Vanderwel & Ganapathisubramani, 2015; Zampiron *et al.*, 2020; Castro & Kim, 2024) with the upwash region located over the ridge crests and the downwash region aligned with the troughs. With a decrease of wave height down to $h/\delta = 0.0195$, the degree of the mean flow field heterogeneity progressively reduces and, as is evident from the in-plane velocity vectors, secondary current vortices become less pronounced until they are almost indiscernible for case 5 (Figure 2c). However, for case 6 (Figure 2d) with the lowest ridge height ($h/\delta = 0.00975$) the degree of the mean flow field heterogeneity increases compared to case 5. Moreover, the secondary current vortices for case 6 are shifted in the spanwise direction, i.e., the upwash and downwash regions are not aligned with crest and trough, respectively.

The contours of magnitude of secondary currents determined as $\sqrt{\overline{v}^2 + \overline{w}^2}/U_b$, where U_b is the bulk flow velocity, are shown in Figure 3. As the ridge height is reduced to $h/\delta = 0.0195$ the magnitude of secondary currents progressively drops (Figures 3a–c), demonstrating a decrease in the strength of secondary currents with a reduction of h. However, higher values of $\sqrt{\overline{v}^2 + \overline{w}^2}/U_b$ are observed for case 6, i.e., the lowest ridge height tested, compared to case 5 (Figure 3d).

As can be observed from the downward shift of the double-averaged streamwise velocity profiles with respect to the smooth-wall case (Figure 4a), the presence of ridges and secondary currents induces a roughness effect, which decreases as h is reduced. This is quantified through the roughness function ΔU^+ computed based on the friction factor (C_f) as $\Delta U^+ = (\sqrt{2/C_f})_s - (\sqrt{2/C_f})_r$ (Granville, 1987), where subscripts 's' and 'r' denote 'smooth' and 'rough' wall, re-

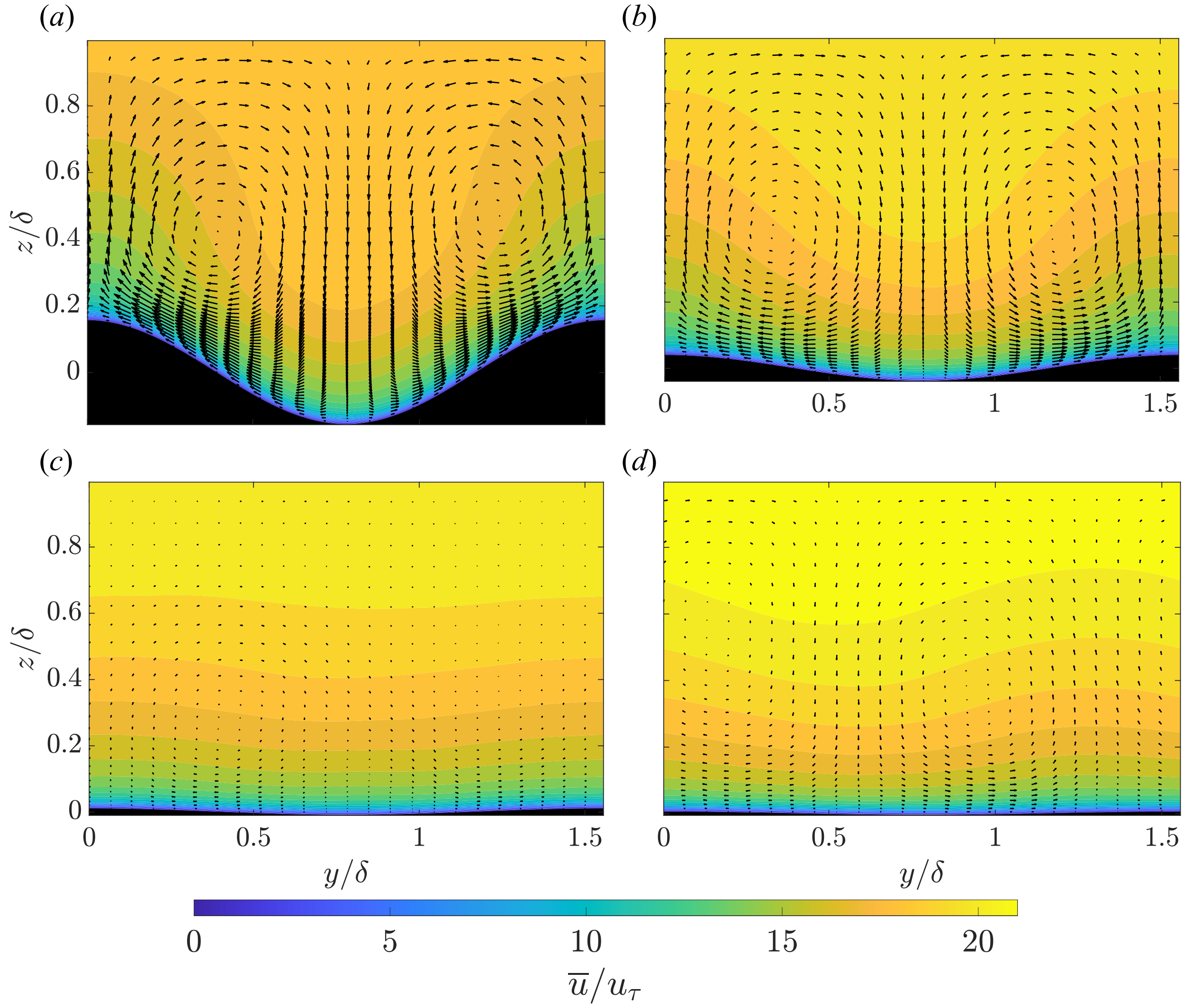

Figure 2. Contours of the phase-averaged mean streamwise velocity with superimposed in-plane velocity vectors, which are down-sampled and scaled for clarity. (a) case 1 ($h/\delta = 0.312$), (b) case 3 ($h/\delta = 0.078$), (c) case 5 ($h/\delta = 0.0195$), and (d) case 6 ($h/\delta = 0.00975$).

spectively, and $C_f = 2(u_\tau/U_b)^2$. ΔU^+ drops almost linearly with a reduction of ridge height down to $h/\delta = 0.0195$ (see inset in Figure 4a); however, extrapolation of this linear fit to $h = 0$ would give a non-zero negative value of ΔU^+. For the lowest tested ridge height $h/\delta = 0.00975$ a departure from this linear behaviour is observed, leading to a slower decrease of the roughness function with h consistent with the recovery of smooth-wall conditions as the ridge height vanishes, i.e., $\Delta U^+ = 0$ for $h = 0$.

The presence of secondary currents also has a significant effect on Reynolds (Figure 4b) and dispersive shear stresses (Figure 4c). Pronounced secondary currents result in a deficit in the Reynolds shear stress compared to the smooth wall case across the entire channel height (Figure 4b). With a reduction of ridge height, the deficit becomes smaller, and for case 5 the $\langle\overline{u'w'}\rangle$ profile closely follows the smooth-wall case the above the ridge crests. However, an increase in the deviations from smooth-wall conditions is observed for case 6, i.e., the lowest ridge height.

The increase in Reynolds shear stress is accompanied by a decrease in $-\langle\tilde{u}\tilde{w}\rangle^+$ (Figure 4c), which almost disappears as $h \to 0$. Dispersive shear stress is widely used as an indicator of secondary current strength. In the inset to Figure 4c the variation of peak magnitude of $-\langle\tilde{u}\tilde{w}\rangle^+$ with h is plotted, showing that, unlike the roughness function, $\langle\tilde{u}\tilde{w}\rangle^+_{\max}$ reduces logarithmically with a decrease in h. However, the trend is broken for the two lowest tested ridge heights, with case 6 ($h/\delta = 0.00975$) showing a higher value of $\langle\tilde{u}\tilde{w}\rangle^+_{\max}$ compared to case 5 ($h/\delta = 0.0195$).

To gain further insight into the behaviour of secondary currents and the observed inconsistencies in the trends in Reynolds and dispersive shear stresses at very low ridge heights, we perform a sliding averaging in time based on snapshots of the instantaneous velocity field separated by 13.75 viscous time units ($\Delta t^+ = \Delta t u_\tau^2/\nu$) that were acquired in each simulation. The sliding average window size is chosen as $\Delta T^{\mathrm{sla}} = 5\delta/u_\tau$, which is sufficiently long to observe secondary current vortices, and the applied sliding shift between successive averages is set to $\Delta T^{\mathrm{shift}} = 1\delta/u_\tau$.

Results of the sliding average are shown for the mean streamwise velocity field together with superimposed in-plane velocity vectors for cases 2 and 5 in Figure 5. For cases with $h/\delta \geq 0.039$ the topology of the secondary current vortices remains consistent for all sliding average windows, with upwash regions observed over the crests and downwash above troughs (see left column in Figure 5, where results for case 2

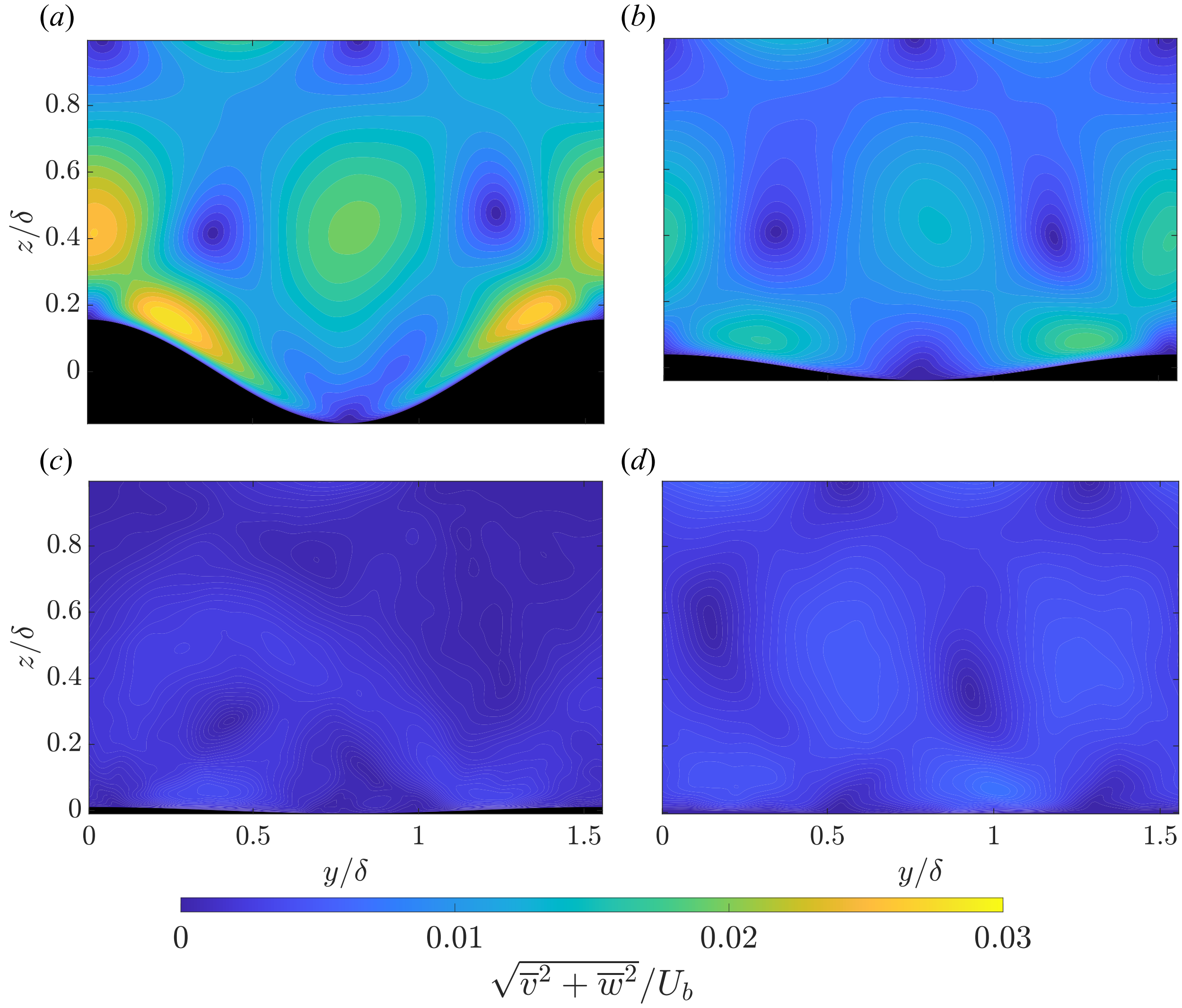

Figure 3. Contours of the phase-averaged magnitude of the secondary currents. (a) case 1 ($h/\delta = 0.312$), (b) case 3 ($h/\delta = 0.078$), (c) case 5 ($h/\delta = 0.0195$), and (d) case 6 ($h/\delta = 0.00975$).

are shown as a representative example). The upwash regions are not strictly vertical, but shift along the curved ridge crest, which is attributed to the chosen geometry that has no singularities that can pin the flow.

In contrast, for cases 5 and 6, which have the lowest tested ridge heights, there are sliding average windows where the topology of secondary currents is reversed, i.e., upwash occurs above the trough and downwash over the crest, suggesting that secondary current vortices are not locked in place by the ridge geometry, due to their low height and smooth shape, and are able to meander in the spanwise direction (see right column in Figure 5, where results for case 5 are shown as a representative example). As a result, the mean flow and turbulence statistics are strongly influenced by the meandering, which does not exhibit a particular pattern, and hence depend on the start and end point in time for time-averaging of the statistics. It should be noted that for the current simulations we used total averaging times of $\Delta T^{\mathrm{ave}} \gtrsim 100\delta/u_\tau$, which gives converged statistics for previous ridge type-roughness studies (e.g., Castro & Kim, 2024; Zhdanov *et al.*, 2024) and for the present cases with high and medium ridge heights. However, the present results suggest that cases with very low ridge heights require significantly longer averaging periods to achieve statistical convergence.

CONCLUSIONS AND OUTLOOK

The influence of ridge height on secondary currents has been investigated for sinusoidal ridges using direct numerical simulations. The chosen ridge geometry is free from singularities such as the corner points found in ridges with rectangular or triangular cross-section, i.e., the studied geometry is continuous and infinitely differentiable and has smoothness properties resembling those of a flat surface.

The studied ridge-type surfaces induce a roughness effect, and the roughness function, ΔU^+, exhibits a close to linear dependence on ridge height over the tested range. The present results suggest that secondary currents can be induced by ridges with heights as low as $h/\delta = 0.00975$ ($h^+ = 5.36$). However, in contrast to cases with taller ridges, for surfaces with ridge heights $h/\delta \leq 0.0195$ ($h^+ \leq 10.72$), the secondary current vortices are not locked in place by the ridges and meander in the spanwise direction. This behaviour leads to time periods in which a reversal of the usual topology of secondary currents is observed, with upwash regions aligned with troughs and downwash regions with crests.

As expected, the strength of secondary currents decreases as the ridge height is reduced, showing an approximately logarithmic dependence of the peak dispersive shear stress on h/δ. However, at very low sine wave amplitudes this trend is not

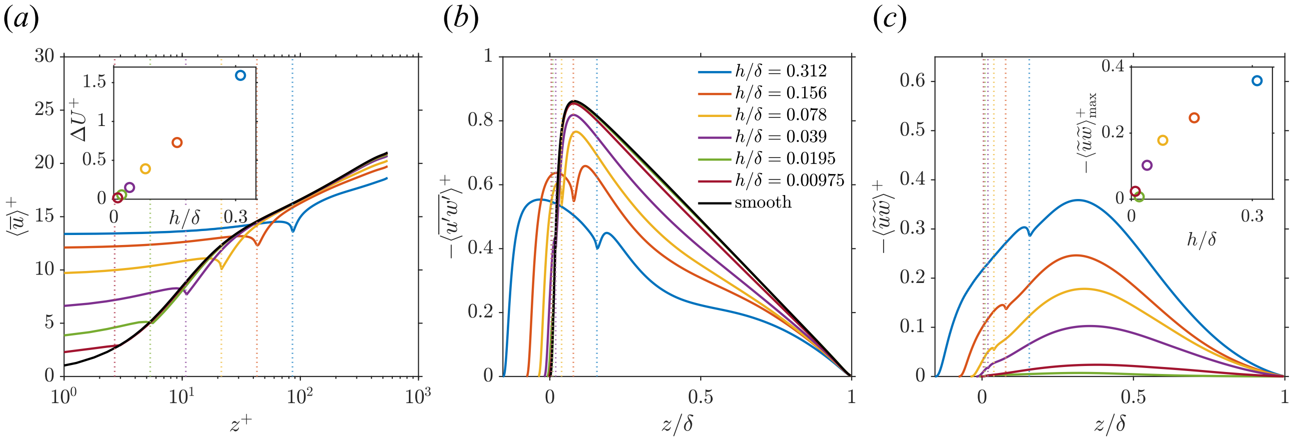

Figure 4. Profiles of (a) streamwise velocity, (b) Reynolds shear stress, and (c) dispersive shear stress for sinusoidal ridge surfaces with varied ridge height. Reference smooth-wall data is shown with black lines. The locations of the ridge crests are marked by thin dotted vertical lines. The legend in part (b) applies to all parts of the figure. The inset in part (a) shows the variation of the roughness function with ridge height. The inset in part (c) shows the variation of the peak magnitude of $-\langle \tilde{u}\tilde{w} \rangle^+$ with ridge height.

clearly observed due to the meandering of the secondary currents. It is therefore conjectured that significantly longer averaging periods are required in these cases to achieve statistical convergence of Reynolds and dispersive stresses, as well as of the strength of secondary currents.

In the limit of infinitely long averaging times and very low ridge height, the spanwise heterogeneity of the mean flow is expected to be significantly reduced or even to vanish. Nevertheless, secondary currents may persist within finite averaging windows. Ongoing work extends the present study by running simulations for the two lowest tested amplitudes further for longer sampling periods with the aim of improving statistical convergence and to clarify the behaviour and persistence of secondary currents as the smooth-wall limit is approached.

ACKNOWLEDGEMENTS

We gratefully acknowledge support for this work by the United Kingdom's Engineering and Physical Sciences Research Council under grant number EP/V002066/1. This work used the ARCHER2 UK National Supercomputing Service (https://www.archer2.ac.uk)(Beckett *et al.*, 2024). The authors gratefully acknowledge the computing time made available to them on the high-performance computer "Lise" at the NHR Center NHR@ZIB. This center is jointly supported by the Federal Ministry of Education and Research and the state governments participating in the NHR (www.nhr-verein.de/unsere-partner).

REFERENCES

Beckett, G., Beech-Brandt, J., Leach, K., Payne, Z., Simpson, A., Smith, L., Turner, A. & Whiting, A. 2024 ARCHER2 service description .

Busse, A., Lützner, M. & Sandham, N.D. 2015 Direct numerical simulation of turbulent flow over a rough surface based on a surface scan. *Computers & Fluids* **116**, 129–147.

Castro, I.P. & Kim, J.W. 2024 Secondary motions in turbulent ribbed channel flows. *Journal of Fluid Mechanics* **988**, A2.

Granville, P.S. 1987 Three indirect methods for the drag characterization of arbitrarily rough surfaces on flat plates. *Journal of Ship Research* **31** (1).

Prandtl, L. 1952 *Essentials of Fluid Dynamics: with Applications to Hydraulics, Aeronautics, Meteorology, and Other Subjects*. Blackie.

Raupach, M.R. & Shaw, R.H. 1982 Averaging procedures for flow within vegetation canopies. *Boundary-Layer Meteorology* **22** (1), 79–90.

Vanderwel, C. & Ganapathisubramani, B. 2015 Effects of spanwise spacing on large-scale secondary flows in rough-wall turbulent boundary layers. *Journal of Fluid Mechanics* **774**, R2.

Wang, Z.-Q. & Cheng, N.-S. 2006 Time-mean structure of secondary flows in open channel with longitudinal bedforms. *Advances in Water Resources* **29** (11), 1634–1649.

Yang, J. & Balaras, E. 2006 An embedded-boundary formulation for large-eddy simulation of turbulent flows interacting with moving boundaries. *Journal of Computational Physics* **215** (1), 12–40.

Zampiron, A., Cameron, S. & Nikora, V. 2020 Secondary currents and very-large-scale motions in open-channel flow over streamwise ridges. *Journal of Fluid Mechanics* **887**, A17.

Zhdanov, O., Jelly, T.O. & Busse, A. 2024 Influence of ridge spacing, ridge width, and reynolds number on secondary currents in turbulent channel flow over triangular ridges. *Flow, Turbulence and Combustion* **112** (1), 105–128.

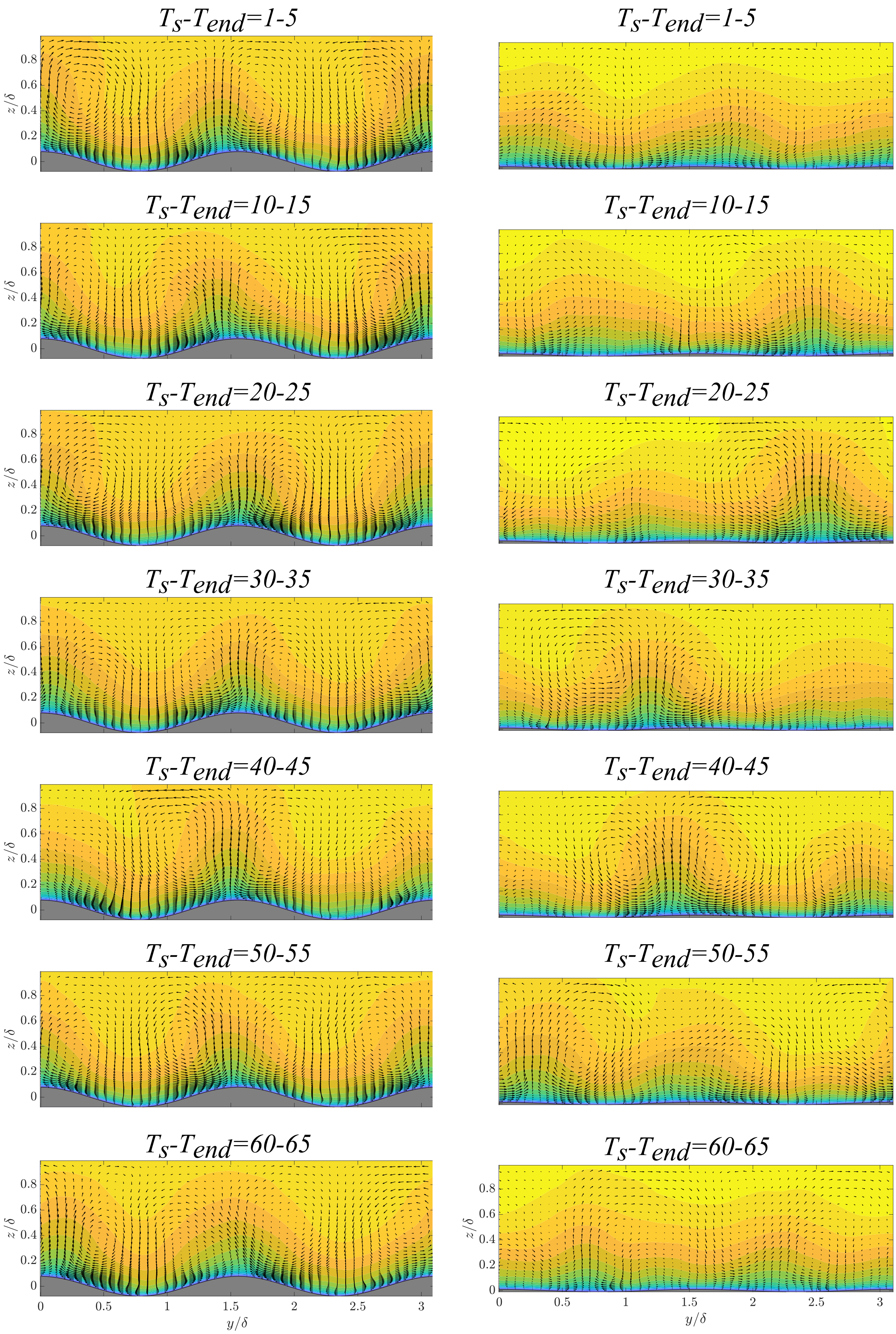

Figure 5. Contours of the streamwise and time-averaged streamwise velocity based on the sliding averaging for a window size of $\Delta T^{\mathrm{sla}} = 5\delta/u_\tau$. Superimposed in-plane velocity vectors are also shown, which are downsampled and scaled for clarity. Left column: case 2 ($h/\delta = 0.156$); right column: case 5 ($h/\delta = 0.0195$). The start (T_{s}) and end (T_{end}) of each time averaging window are indicated above the corresponding panel.